Comparison of Bulk Piezoelectric and Opto-Mechanical Micromachined Detectors for Optoacoustic and Ultrasound Sensing

A. Prebeck, G. Keulemans, U. Stahl, H. Jans, X. Rottenberg, V. Ntziachristos

Abstract— Optical detection of sound, using opto-mechanical micromachined ultrasound sensors (OMUS), is a promising detection technology for optoacoustic (OptA) imaging because it achieves a small active detection area, in the few tens of micrometers size, without loss of sensitivity as a function of area size. It also has potential to be produced as array configurations at low cost. However, while OMUS sensitivity has been reported in terms of noise equivalent pressure density (NEPD), there has been no comparison to conventional piezoelectric transducers under identical conditions. We differentially compared a highly sensitive ring-resonator-based OMUS and a single element focused piezoelectric ultrasound transducer (FPUT), under the same experimental conditions. The comparison considered the detectors' signal-to-noise ratio (SNR), impulse response, axial point-spread-function and their spatial sensitivity. Our results show that OMUS attained lower SNR to FPUT, when operating at the same working distance, but similar performance when placed close to the sample interrogated, for example as it relates to optoacoustic microscopy. Advantageously, OMUS uniquely offers the spatial behavior of a point-like acoustic detector which reduces the sensitivity to ultrasound interference effects occurring on the large detection area of FPUTs. We discuss the implications of the two detection approaches in the design of OptA systems.

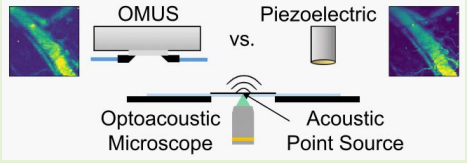

Index Terms— Application Characterization, Comparative Characterization, OMUS, Photoacoustic Microscopy, Photoacoustic Sensing

I. Introduction

OPTO-MECHANICAL micromachined ultrasound sensors (OMUS) have emerged as promising detectors for optoacoustic (OptA) imaging and sensing. All optical detection of ultrasound achieves sensitivity that is essentially independent of the detector size and can lead to steep miniaturization over piezoelectric ultrasound elements [1]. Additionally, advances in integrated photonics technology have made it possible to reliably manufacture photonic structures using processes established in semiconductor mass production [2, 3]. This development could allow for parallel processing of multiple OMUS on a single substrate, enabling dense array configurations and reducing production cost compared to piezoelectric transducers. With a noise performance competitive to that of current state-of-the-art single element focused piezoelectric ultrasound transducers (FPUTs), the OMUS technology could become the method of choice in OptA system implementations.

Various noise equivalent pressure density (NEPD) values for opto-mechanical ultrasound sensors [4–16] and piezoelectric detectors [17, 18] have been reported (see Table I). These reported values have been used to compare opto-mechanical sensors among themselves [1, 2, 19–21], as well as against commercially available piezoelectric transducers [1]. These comparisons show that OMUS' absolute NEPD can be competitive with the NEPD of FPUTs. However, such comparisons are based on literature values that originate from different characterization systems and techniques. Theoretical calculations of the NEPD of the reported most sensitive ring-resonator-based OMUS show that the OMUS could surpass piezoelectric ultrasound transducers in two specific scenarios [22]. The first scenario is in OptA microscopy and sensing, if the OMUS can be placed close to the acoustic source (less than 0.2 mm to 2 mm in distance, depending to which conventional transducer it is compared). The second scenario is in OptA tomography, if the spatial Nyquist criterion limits the largest possible size of individual detector elements in a transducer element array (which is shown theoretically to occur

This project has received funding from the European Union's Horizon 2020 research and innovation programme under grant agreement No 862811 (RSENSE) and the European Union's Horizon Europe research and innovation programme under grant agreement No 101058111 (GLUMON). This research is (partially) funded by Imec's strategic innovation program: Invest+.

A. Prebeck (alexander.prebeck@tum.de), U. Stahl (uli.stahl@tum.de) and V. Ntziachristos (**bioimaging.translatum@tum.de**) are with the Chair of Biological Imaging, Central Institute for Translational Cancer Research (TranslaTUM), School of Medicine and Health & School of Computation, Information and Technology, Technical University of Munich, Munich, Germany and Institute of Biological and Medical Imaging, Bioengineering Center, Helmholtz Zentrum München, Neuherberg, Germany. Additionally, V. Ntziachristos is with Munich Institute of Biomedical Engineering (MIBE), Technical University of Munich, Garching b. München, Germany and Institute of Electronic Structure and Laser (IESL), Foundation for Research and Technology Hellas (FORTH), Heraklion, Greece.

G. Keulemans (grim.keulemans@imec.be), H. Jans (hilde.jans@imec.be) and X. Rottenberg (xavier.rottenberg@imec.be) are with Imec, Leuven, Belgium.

for arrays of the OMUS with half-wavelength element pitch at acoustic frequencies higher than 2.5 MHz). However, without knowing a piezoelectric transducer's exact physical parameters in order to make these calculations, a true comparison between the OMUS and a piezoelectric transducer is not possible. Furthermore, electromagnetic interference in the OptA system, which is not modelled in the calculations, can significantly undermine a detector's sensitivity within the system. Despite this promising outlook, OMUS's performance has not yet been compared to the performance of FPUTs under identical experimental conditions. Thus, it is not yet clear how OMUS' and FPUTs reported noise performance and sensitivity compare to each other.

We investigated the performance of the most sensitive OMUS reported, operating in the frequency range of 3-30 MHz, which is based on a highly sensitive waveguide arrangement that implements a membrane suspended above a ring resonator [16], a design that is miniaturized (11 µm ring diameter) and can be mass-produced for widespread use in OptA imaging [16, 23]. To compare the OMUS in the context of OptA imaging of microvasculature, we further investigated the performance of three FPUTs that could be used in raster scan optoacoustic mesoscopy (RSOM), including two broadband Lithium Niobate ($LiNbO_3$) transducers with center frequencies of 25 MHz and 50 MHz respectively, as well as a less broadband 25 MHz piezocomposite transducer to match the center frequency and bandwidth of the OMUS. RSOM, one of the most commonly used OptA imaging modalities in large medical studies [24, 25], visualizes microvasculature in skin and typically operates in the frequency range of 10-40 MHz to visualize larger vessels, as well as in the range of 40-120 MHz for visualization of small features like capillary loops or melanin deposits [26–29].

In previous reports, the OMUS was characterized using a planar acoustic wave generated by a 3 mm wide planar piezoelectric transducer [16], which is a valid noise characterization method for a point-like detector [30]. Unlike OMUS, FPUTs are affected by interference, due to their large detection area, when excited with a wavefront that is not spherical or not originating from the FPUTs' focal point [31]. Hence, noise characterization with an acoustic point source is necessary. Furthermore, sampling the spatial impulse response of an ultrasound detector requires the use of acoustic sources that are smaller than the detectors' acoustic focus, i.e., sub-resolution, and more broadband than the detectors' frequency response [30, 32]. Thus, to accurately compare OMUS and FPUTs, both must be characterized using the same sub-resolution broadband acoustic point source.

We hypothesize that characterizing an OMUS and FPUTs within the same OptA system using the same broadband acoustic point source would result in a valid comparison between these detector elements, allowing us to determine whether and under what circumstances the OMUS performs better than FPUTs for OptA imaging and sensing.

Here, we present a detailed comparison between the most sensitive ring-resonator-based OMUS and FPUTs, the current state-of-the-art ultrasound sensors for OptA microscopy and sensing, under the same conditions using the same broadband acoustic point source. We discuss when replacing a FPUT with an OMUS could be a valid option to bring down OptA system cost, advancing adoption of OptA technology in medical research and practice.

II. Methods

A. Experimental Setup

The broadband acoustic point source used to characterize the OMUS and the FPUTs was created in a custom optical resolution OptA microscope, using the OptA effect (Fig. 1). Light from a diode pumped solid state laser (Flare PQ HP GR 2k-500, Innolight, Germany) with a wavelength of 515 nm, repetition rate of 1.2 kHz and a pulse width of 1.2 ns was first adjusted in its power using a neutral density filter as well as a combination of a rotating polarizer and a polarizing beam splitter, to provide sufficient acoustic pressure for the characterization measurements while still operating the OMUS in a linear regime. After spatially cleaning and expanding the beam with a telescope, the light was focused onto a 110 µm thin black vinyl tape by means of the microscope objective (PLN 10x, NA 0.25; Olympus, Germany). The average power before the objective was measured to be approximately 200 µW using a power meter with a photodiode sensor (PM100D S120C, Thorlabs, Germany).

The optical readout circuit for the OMUS was realized using a continuous wave laser (Intun TLX-1550B, Thorlabs, Germany) with a wavelength tuning range of 1520-1630 nm and a linewidth of 150 kHz. The laser's output was coupled to the OMUS chip via a fiber polarization controller (FPC032, Thorlabs, Germany) and a circulator configured as an optical isolator (CIR1550PM-APC, Thorlabs, Germany). The light transmitted through the OMUS chip was detected by a balanced photodetector (PDB480C, Thorlabs, Germany) and the signal was digitized using a data acquisition card (CS12502, GaGe, USA) interfaced by custom MATLAB code. A silicon photodiode (DET36A, Thorlabs, Germany) detecting scattered light from the diode pumped solid state laser provided a trigger pulse for the acquisition. In the case of the FPUTs, the optical readout circuit was replaced by a bias-tee to supply the transducers' internal pre-amplifier. The signal output of the bias-tee was directly connected to the acquisition card.

B. Ultrasound Detectors

The FPUTs used for the comparison were custom-made spherically focused transducers with either a piezocomposite or a $LiNbO_3$ sensitive element and an integrated 30 dB amplifier. Nominal center frequencies were 25 MHz for the piezocomposite transducer and for the two $LiNbO_3$ transducers 25 MHz and 50 MHz, respectively. The piezocomposite transducer was geometrically focused while the $LiNbO_3$ transducers were focused by an acoustic lens. Each transducer provided a 4 mm focal length as well as a 4 mm wide aperture. The OMUS sample used for the comparison was a device of 20 µm diameter provided by IMEC (Leuven, Belgium). The

OMUS chip was fixed on an aluminum submount to provide acoustic backing. A detailed description of the OMUS used for this study as well as the optical readout scheme can be found elsewhere [16].

C. Impulse Response and Signal-to-Noise Ratio

For the impulse response and signal-to-noise ratio (SNR) measurements, the detectors were acoustically coupled to the broadband acoustic point source by water in a basin. The position of the detectors relative to the point source was adjusted by optimizing the OptA signal amplitude in a raster-scan in the X-Y-Z (FPUT) or X-Y (OMUS) coordinate planes. While the axial distance of the FPUTs to the point source was chosen by signal optimization because of the focused nature of the FPUTs, the OMUS was placed at an axial distance matching the 4 mm working distance of the FPUTs. 100 000 raw OptA A-Lines were recorded for all detectors. To estimate the axial point spread function (PSF), all transients were averaged and the magnitude of the analytic signal for the transients was calculated to create a signal envelope, respectively. The width of the PSF was subsequently estimated as the full-width-half-maximum (FWHM) of the signal envelope, which was mapped from a time-difference Δt to the width of the PSF w_{PSF} by assuming a speed of sound c_{SOS} of 1500 m/s as

$$w_{PSF} = \Delta t \, c_{SOS}. \tag{1}$$

For the SNR estimation, the signal component was isolated by applying a rectangular window function only to the transients within the raw A-Lines, while the noise component was isolated by applying a rectangular window function to the system noise preceding the transients. The power spectral density (PSD) was then calculated by use of Welch's method and the SNR was determined as

$$SNR(f) = 10\text{dB}\, log_{10}\left(\frac{PSD_{Sig}(f)}{PSD_{Noise}(f)}\right) \tag{2}$$

with $PSD_{Sig}(f)$ and $PSD_{Noise}(f)$ as the frequency resolved PSD of the signal- and noise-components, respectively. The frequency of highest SNR was subsequently determined for every transducer.

D. Spatial Sensitivity Measurements

For the spatial sensitivity measurements, the detectors were acoustically coupled and aligned as described for the impulse response and SNR measurements. The detectors were subsequently scanned along the X and Z axes in 10 µm steps for a total of 800 µm in each direction. For each position, 150 A-Lines were recorded and averaged. The signal intensity for each position was determined as the maximum value of the signal envelope calculated by determining the magnitude of the analytic signal.

E. Extrapolating the OMUS' SNR close to the Acoustic Source

The OMUS' SNR in close proximity to the acoustic source was extrapolated from the peak SNR measurement of section II-C. The pressure p of a spherical wave relates to the distance r to the acoustic source as [22]

$$p \propto 1/r. \tag{3}$$

Assuming a spherical wave and assuming the OMUS to be a point-like pressure detector, the measured signal amplitude V of the OMUS relates to the pressure p and thus the distance to the acoustic source r as

$$V \propto p \propto 1/r. \tag{4}$$

The improvement in SNR at distance r to the source was determined as

$$\Delta SNR_r = SNR_r - SNR_{r_0} = 20\text{dB}\, log_{10}(r_0/r) \tag{5}$$

relative to the peak SNR measured at distance r_0, SNR_{r_0}.

F. Imaging Experiment on Mouse Ear ex-vivo

For the imaging experiment, the detectors were aligned using a broadband acoustic point source before inserting a mouse ear, which was fixed to a microscopy slide, into the microscope. The OMUS was operated at a working distance of approximately 4 mm. Acoustic coupling to the sample was achieved using a drop of water. After selecting a region of interest, the sample was raster-scanned in the X-Y plane in 10 µm steps to cover a field of view of 500 µm × 500 µm. For image formation, the signal intensity for each position was determined as the peak-to-peak amplitude of the OptA signal. To calculate a contrast-to-noise ratio (CNR), we selected a 50 µm × 50 µm region inside a high-intensity feature along with a second square region of identical size that was assumed to contain only background noise. The CNR was subsequently determined as

$$CNR = \frac{\bar{X}_{Feature} - \bar{X}_{Noise}}{\sigma_{Noise}} \tag{6}$$

with $\bar{X}_{Feature}$ and $\bar{X}_{Noise}$ being the mean intensities within the corresponding regions and σ_{Noise} being the standard deviation of the noise region.

For each micrograph, a B-plane was extracted to create side-view images. The B-plane image was formed by plotting the analytic signal's magnitude for each A-line within the B-plane.

The mouse ear was taken in secondary use from a recently sacrificed, approximately 8 week-old female athymic nude mouse, Crl:NU(NCr)-Foxn1nu (Charles River Laboratories, Sulzfeld, Germany).

III. Results

A. The OMUS has lower SNR than the FPUTs and offers limited axial resolution

To provide a valid comparison between the detector elements, we characterized the OMUS as well as three different FPUTs using the same broadband acoustic point source in an optical resolution OptA microscope (see section II-A). All

detectors were operated at a comparable working distance. Fig. 2 shows a comparison between the impulse response of the OMUS and the FPUTs. Fig. 2a depicts raw OptA transients (single shot), while Fig. 2b depicts the impulse response calculated after averaging to remove uncorrelated noise. Additionally, Fig. 2b shows an estimate of the axial acoustic PSF, which was determined by calculating the magnitude of the analytic signal of the averaged signal transients. Assuming a speed of sound in water of 1500 m/s, the width of the PSF was estimated as the FWHM of the magnitude of the analytic signal, yielding a PSF with a width of 135 μm for the OMUS and PSFs with widths between 18-66 μm for the FPUTs. The wider PSF of the OMUS would lead to limited axial resolution in an OptA system when the OMUS is used as a detector. Furthermore the data plotted in Fig. 2a suggest that the raw OptA transient recorded by the OMUS is significantly noisier when compared to the transients recorded by the FPUTs.

In Fig. 3, we show a more sophisticated comparison of the noise performance of the individual detectors by comparing the PSD of the raw transient with the PSD of noise preceding the transient. Fig. 3a shows the PSD of the impulse response as well as the peak SNR of the OMUS in the frequency domain, while Figs. 3b-d show the PSDs and peak SNRs of the three FPUTs, also in the frequency domain. The OMUS shows a peak SNR of 11 dB, while the peak SNRs of the FPUTs range from 23-36 dB. In contrast to the flat noise floor of the FPUTs, the PSD of the OMUS' noise- and signal-components clearly follow the same underlying systematics, indicating that the OMUS is limited by acoustomechanical noise. Furthermore, the bandwidths of the FPUTs in the frequency domain correlate well with the PSF results from Fig. 2b with the more broadband transducers providing the tighter PSF.

B. The OMUS offers the spatial characteristics of a point-like detector

Fig. 4 compares the spatial characteristics of the OMUS and the FPUTs. Fig. 4a shows slices through the sensitivity field of the three FPUTs tested in this study. Fig. 4b depicts the lateral sensitivity of the three FPUTs and the OMUS, while Fig. 4c depicts the axial sensitivity of all four detectors. The geometrically-focused 25 MHz piezocomposite transducer produces an acoustic focus that is broader laterally and longer axially than that of the lens-focused $LiNbO_3$ transducers. The axial extension of the acoustic focus of both $LiNbO_3$ transducers is comparable. However, in agreement with the focusing limit of acoustic diffraction, the lateral dimension of the acoustic focus decreases as the center frequency and bandwidth of the transducer increases. In contrast, the OMUS acts as a point-like detector with a sensitivity that is barely dependent on the position of the acoustic point source relative to the detector. In these measurements, the OMUS was placed at the same working distance (~4 mm) as the FPUTs.

Because the OMUS functions as a point-like detector, it does not rely on a focusing mechanism and thus can provide measurements of signal amplitude that are essentially insensitive to small changes in distance between the acoustic source and the detector. We can also exploit the point-like behaviour of the OMUS by bringing it very close to the acoustic source, increasing its SNR. Fig. 5 extrapolates the OMUS' peak SNR obtained in the measurements of Fig. 3 under the assumption of a point-detector and a spherical wave created by the acoustic point source. Under those assumptions, we show that when placed close to the acoustic source, the OMUS could potentially outperform the peak SNRs of all three FPUTs, which are bound to their focusing distances. The SNR crossover point, i.e. the distance at which the OMUS starts outperforming the individual FPUTs, lies between 0.2 mm to 1.0 mm, depending on the respective FPUT to which it is compared.

C. OMUS and FPUT perform comparably in optical resolution OptA microscopy

Fig. 6 compares two micrographs of vasculature inside a mouse ear recorded ex-vivo using either the OMUS operated at a long working distance (Fig. 6a) or the 25 MHz piezocomposite FPUT (Fig. 6b), which is the FPUT most similar to the OMUS in frequency response. The lower peak SNR of the OMUS likely contributes to the loss of small, low-intensity features in the OMUS micrograph compared to the FPUT micrograph (red arrows). Quantifying this decrease in contrast by calculating a contrast-to-noise ratio (CNR) between the vessel and the background next to the vessel yields a CNR of 74 for the OMUS and a CNR of 194 for the FPUT. However, even with the lower CNR of the OMUS, the features visible in both micrographs are essentially comparable.

Side views acquired at the middle of the micrographs show that the OMUS (Fig. 6c), due to its lower bandwidth and consequent wider PSF, smooths axial features more than the FPUT (Fig. 6d). The FPUT shows lower signal intensity in deeper vessels due to its limited depth-of-field. In contrast, the OMUS, being a point-like detector, has a larger depth-of-field, resulting in signal intensities that are less affected by vessel depth.

D. Summary of characterization results

Table II summarizes the characterization results obtained from the individual sensors. Although the OMUS has an active area several orders of magnitude smaller than that of the FPUTs, its SNR is at most 25 dB lower, corresponding to approximately one order of magnitude difference in signal amplitude. As a membrane-based device working near its fundamental acousto-mechanical resonance, the OMUS shows a lower fractional bandwidth compared to the FPUTs. The axial PSF of the OMUS is 2 times wider compared to the 25 MHz piezocomposite transducer and 4 times wider compared to the 25 MHz LiNbO3 transducer.

A comparison among the FPUTs shows that the piezocomposite detector exhibits up to 13 dB higher SNR, albeit at the cost of up to 73% lower fractional bandwidth, translating to a 4 times wider axial PSF. Additionally, the piezocomposite detector exhibits the largest acoustic focus, with a focal length and width up to double that of the LiNbO3 transducers.

IV. Discussion

In this work, we compared a ring-resonator-based OMUS and three FPUTs using the same experimental arrangement and broadband acoustic point source. We observed that the FPUTs

and the OMUS exhibited strong differences in noise performance as well as in spatial sensitivity. However, when implemented within the same optical resolution OptA microscopy setup, the micrographs recorded using the individual detectors were essentially comparable. Our study represents the first valid experimental comparison between this OMUS and the state-of-the-art FPUTs for OptA microscopy and sensing. The work provides a framework for system designers, enabling them to balance scientific requirements with physical and financial limitations in order to make informed decisions about which detector to implement in a particular OptA system.

When characterized using the same broadband acoustic point source, the OMUS showed a wider axial PSF, i.e., lower axial resolution, than the FPUTs. These results suggest that a FPUT is better suited for systems that require high axial resolution. The limited axial resolution for the OMUS when compared to the FPUTs is partially expected based on estimates of axial resolution from the OMUS's developers, who report a 16.4 MHz full FWHM bandwidth for their device [16], enabling an axial resolution of ~80 µm ($w_{PSF} = 0.88\, c/B$; w_{PSF}: FWHM of point spread function, c: speed of sound, B: signal bandwidth [33]). This reported axial resolution is lower than any of the FPUTs results, however, our measured axial resolution of 135 µm for the OMUS is still lower than previously reported values [16, 23]. The wider PSF of our OMUS sample when compared to results from the literature could be attributed to non-optimal acoustic backing in our sample, resulting in internal acoustic reflections and thus an artificially widened PSF. Furthermore, the axial resolution of the OMUS device could be increased in the future by optimizing its membrane design, i.e. optimizing the membrane's mechanical properties by changing its diameter, layer thickness as well as internal stress [23].

We further observed that when operated at a long working distance (i.e., at a similar working distance to the FPUTs), the sensitivity of the OMUS was barely dependent on the position of the acoustic source relative to the detector. Thus, the OMUS behaves as a point-like detector, which is expected considering its small dimensions relative to the acoustic wavelengths to which it is sensitive. The observed insensitivity of the OMUS to displacements matches previous characterization results which report a signal intensity within a 30 % tolerance window for angles of incidence up to 60° [16], and makes the OMUS well suited for OptA systems implementing an off-axis configuration, e.g., for large field-of-view microscopy with a stationary detector [34, 35]. The OMUS would also be ideal for depth-of-field optimized microscopy systems using elongated needle-shaped beams, as the long needle-shaped optical focus often does not match the short acoustic focus of typical FPUTs [36, 37].

However, at such long working distances, the OMUS displayed a lower peak SNR compared to the FPUTs. Thus, if an OptA system requires high SNR and relies on a larger acoustic working distance, FPUTs are better suited as detectors. In contrast to FPUTs, which are sensitive to noise contributions from their focal volume, the OMUS as an omnidirectional sensor effectively couples to all noise contributions in the half-space above the sensor, decreasing the OMUS' SNR. Furthermore, the limited SNR of the OMUS is consistent with theoretical calculations which suggest that the OMUS is only able to surpass FPUTs in NEPD when operated closer than 2 mm from a point-like source [22]. Indeed, when we extrapolated from our measured data, we found that the SNR of the OMUS increased with shorter distances to the acoustic source, surpassing the best possible peak SNR of the individual FPUTs at distances ranging from 0.2 mm to 1.0 mm to the acoustic source, depending on the specific FPUT. The crossover distance for the tested FPUTs thus lay within the theoretical interval given in the literature (Fig. 5). This enhanced SNR at short distances to the acoustic source could progress fields where reduced noise levels are of great importance, e.g., in non-invasive OptA monitoring of metabolites [38].

When integrated into the same optical resolution OptA microscopy setup, micrographs obtained by the OMUS displayed a lower CNR than micrographs obtained using the FPUT most comparable to the OMUS (25 MHz piezocomposite, Fig. 6). We further observed that micrographs recorded with the OMUS lost small, low intensity features, which were visible in the micrograph obtained using the FPUT. However, for larger, high-contrast features, micrographs recorded using the OMUS and the FPUT were essentially comparable. As the lateral resolution in optical resolution OptA microscopy is determined by the optical system, comparable lateral resolution of the micrographs is expected. The difference in CNR can be attributed to the OMUS' lower SNR, while the loss of small features when using the OMUS can be explained by a combination of the OMUS' lower SNR and limited bandwidth. Small features result in high-frequency components, to which OMUS is less sensitive when compared to the more broadband FPUT. This suggests that systems, targeting such small, low intensity features will profit from integrating an FPUT, but systems targeting larger features can use an OMUS to acquire functionally comparable micrographs.

The OMUS achieves a comparable sensitivity with a detection area that is multiple orders of magnitude smaller than that of piezoelectric detectors, whose sensitivity is proportional to their respective detection area. Despite the significant difference in size, the OMUS exhibits a NEPD only 1 to 2 orders of magnitude higher than those of commercially available and recently reported piezoelectric detectors (see Table I).

Compared among recently reported photonic ultrasound detectors, the silicon OMUS detector characterized in this study achieves the lowest NEPD, although it displays a smaller fractional bandwidth (see Table I). The limited bandwidth of the OMUS stems from the high acousto-mechanical quality factor of its internal membrane when operated in liquid, a characteristic that is absent in the other photonic detectors. Additionally, ring resonator-based photonic ultrasound detectors like OMUS can be easily arranged in two-dimensional arrays, which is not straightforward for Bragg grating-based systems [5, 12]. Furthermore, silicon photonics technology benefits from compatibility with standard complementary metal-oxide semiconductor (CMOS) fabrication infrastructure,

offering scalability and cost advantages that are not easily achieved with more exotic materials such as chalcogenides [11]. While photonic ultrasound sensors based on silicon nitride ring resonators have also been demonstrated [10], they have yet to achieve the NEPD values reported for the silicon based OMUS characterized in this work [16].

State-of-the-art piezoelectric optoacoustic detectors typically require only the integration of a pre-amplifier, allowing direct connection to a high-sample-rate data acquisition system via a 50-Ohm cable, without significantly altering the sensitivity. In contrast, current opto-mechanical ultrasound sensors still rely on high-end and expensive benchtop lasers and photodetectors for a read-out, as the indirect band gaps of silicon prohibit efficient lasing. Over the past few decades, several approaches for introducing III/V materials for light emission in silicon photonics have been investigated, including hybrid integration using wafer bonding, flip-chip technology, micro-transfer printing (μTP), and monolithic integration by hetero-epitaxial growth [39]. While μTP has been available in laboratory settings for over a decade, it is now approaching maturity for use in mass-produced photonic devices [40]. Additionally, recent advancements have shown full wafer-scale fabrication of GaAs-based nano-ridge lasers [41]. The large-scale integration of lasers and detectors will enable future on-chip photonic read-out and signal conversion and significantly reduce system complexity when using opto-mechanical ultrasound detection.

Our study provides the first experimental comparison of the OMUS and a comparable FPUT in an optical resolution OptA microscopy setting, instead of inferring imaging performance from NEPD values published in the literature. However, while our results apply in an optical resolution OptA microscopy setting, they might not be directly translatable to other applications like OptA tomography. This can be addressed in future studies which perform dedicated characterizations and comparisons for other targeted applications. For example, the OMUS could be promising for optical resolution OptA microscopy using mid-infrared light sources. OptA mid-infrared spectroscopy typically suffers from the low output power of quantum cascade lasers, which could be compensated for by leveraging the superior SNR of the OMUS when operated at a short working distance. Additionally, the superior SNR of the OMUS when placed close to the acoustic source has only been shown under the assumption that both the detector and the acoustic source are point-like. A dedicated characterization close to the acoustic near-field could experimentally validate this extrapolation.

V. Conclusion

In summary, while the OMUS exhibits a lower SNR and reduced axial resolution compared to FPUTs under certain conditions, its performance in the same OptA system is essentially comparable. As such, the limitations of OMUS may be outweighed by its physical and cost advantages.

Given the scalability of OMUS production, its integration could enable the widespread adoption of OptA systems in clinical settings by considerably reducing the cost of OptA systems. Furthermore, potential for high SNR and the compact size of OMUS make it well-suited for incorporating into high-density detector arrays. This could enable breakthroughs in currently challenging applications, such as functional brain imaging through the skull or non-invasive measurements of metabolites in the skin.

Acknowledgment

This project has received funding from the European Union's Horizon 2020 research and innovation programme under grant agreement No 862811 (RSENSE) and the European Union's Horizon Europe research and innovation programme under grant agreement No 101058111 (GLUMON). This research is (partially) funded by Imec's strategic innovation program: Invest+

We thank Dr. Hailong He for providing us with the custom piezoelectric transducers characterized in this study. Furthermore, we thank Dr. Elisa Bonnin for her attentive reading and improvements of the manuscript.

Conflict of Interest

V.N. is a founder and equity owner of Maurus OY, sThesis GmbH, iThera Medical GmbH, Spear UG and I3 Inc. The remaining authors declare no conflicts of interest.

References

[1] G. Wissmeyer, M. A. Pleitez, A. Rosenthal, and V. Ntziachristos, "Looking at sound: optoacoustics with all-optical ultrasound detection," *Light, science & applications*, vol. 7, p. 53, 2018, doi: 10.1038/s41377-018-0036-7.

[2] X. Cao, H. Yang, Z.-L. Wu, and B.-B. Li, "Ultrasound sensing with optical microcavities," *Light, science & applications*, vol. 13, no. 1, p. 159, 2024, doi: 10.1038/s41377-024-01480-8.

[3] N. Quack *et al.,* "Integrated silicon photonic MEMS," *Microsystems & nanoengineering*, vol. 9, p. 27, 2023, doi: 10.1038/s41378-023-00498-z.

[4] Z. Ding, J. Sun, C. Li, and Y. Shi, "Broadband Ultrasound Detection Using Silicon Micro-Ring Resonators," *J. Lightwave Technol.*, vol. 41, no. 6, pp. 1906–1910, 2023, doi: 10.1109/JLT.2022.3227064.

[5] Y. Hazan, A. Levi, M. Nagli, and A. Rosenthal, "Silicon-photonics acoustic detector for optoacoustic micro-tomography," *Nature communications*, vol. 13, no. 1, p. 1488, 2022, doi: 10.1038/s41467-022-29179-7.

[6] G. J. Hornig, K. G. Scheuer, E. B. Dew, R. Zemp, and R. G. DeCorby, "Ultrasound sensing at thermomechanical limits with optomechanical buckled-dome microcavities," *Optics express*, vol. 30, no. 18, pp. 33083–33096, 2022, doi: 10.1364/OE.463588.

[7] T. A. La, O. Ülgen, R. Shnaiderman, and V. Ntziachristos, "Bragg grating etalon-based optical fiber for ultrasound and optoacoustic detection," *Nature communications*, vol. 15, no. 1, p. 7521, 2024, doi: 10.1038/s41467-024-51497-1.

[8] Y. Lee *et al.,* "Theoretical and experimental study on the detection limit of the micro-ring resonator based

ultrasound point detectors," *Photoacoustics*, vol. 34, p. 100574, 2023, doi: 10.1016/j.pacs.2023.100574.

[9] J. Ma, J. Zhao, H. Chen, L.-P. Sun, J. Li, and B.-O. Guan, "Transparent microfiber Fabry-Perot ultrasound sensor with needle-shaped focus for multiscale photoacoustic imaging," *Photoacoustics*, vol. 30, p. 100482, 2023, doi: 10.1016/j.pacs.2023.100482.

[10] M. Nagli *et al.,* "Silicon photonic acoustic detector (SPADE) using a silicon nitride microring resonator," *Photoacoustics*, vol. 32, p. 100527, 2023, doi: 10.1016/j.pacs.2023.100527.

[11] J. Pan *et al.,* "Parallel interrogation of the chalcogenide-based micro-ring sensor array for photoacoustic tomography," *Nature communications*, vol. 14, no. 1, p. 3250, 2023, doi: 10.1038/s41467-023-39075-3.

[12] R. Shnaiderman, G. Wissmeyer, O. Ülgen, Q. Mustafa, A. Chmyrov, and V. Ntziachristos, "A submicrometre silicon-on-insulator resonator for ultrasound detection," *Nature*, vol. 585, no. 7825, pp. 372–378, 2020, doi: 10.1038/s41586-020-2685-y.

[13] Y. Tong *et al.,* "Ultrafast optical phase-sensitive ultrasonic detection via dual-comb multiheterodyne interferometry," *Advanced Photonics Nexus*, vol. 2, no. 01, 2023, doi: 10.1117/1.APN.2.1.016002.

[14] O. Ülgen, R. Shnaiderman, C. Zakian, and V. Ntziachristos, "Interferometric optical fiber sensor for optoacoustic endomicroscopy," *Journal of biophotonics*, vol. 14, no. 7, e202000501, 2021, doi: 10.1002/jbio.202000501.

[15] H. Yang *et al.,* "Micropascal-sensitivity ultrasound sensors based on optical microcavities," *Photon. Res.*, vol. 11, no. 7, p. 1139, 2023, doi: 10.1364/PRJ.486849.

[16] W. J. Westerveld *et al.,* "Sensitive, small, broadband and scalable optomechanical ultrasound sensor in silicon photonics," *Nat. Photonics*, vol. 15, no. 5, pp. 341–345, 2021, doi: 10.1038/s41566-021-00776-0.

[17] A. Kurnikov, A. Sanin, X. L. D. Ben, D. Razansky, and P. Subochev, "Ultrawideband sub-pascal sensitivity piezopolymer detectors," *Ultrasonics*, vol. 141, p. 107349, 2024, doi: 10.1016/j.ultras.2024.107349.

[18] S. Cho *et al.,* "An ultrasensitive and broadband transparent ultrasound transducer for ultrasound and photoacoustic imaging in-vivo," *Nature communications*, vol. 15, no. 1, p. 1444, 2024, doi: 10.1038/s41467-024-45273-4.

[19] N. L. Kazanskiy, S. N. Khonina, and M. A. Butt, "A Review of Photonic Sensors Based on Ring Resonator Structures: Three Widely Used Platforms and Implications of Sensing Applications," *Micromachines*, vol. 14, no. 5, 2023, doi: 10.3390/mi14051080.

[20] Y. Lee, H. F. Zhang, and C. Sun, "Highly sensitive ultrasound detection using nanofabricated polymer micro-ring resonators," *Nano convergence*, vol. 10, no. 1, p. 30, 2023, doi: 10.1186/s40580-023-00378-2.

[21] L. Zhu, H. Cao, J. Ma, and L. Wang, "Optical ultrasound sensors for photoacoustic imaging: a review," *Journal of biomedical optics*, vol. 29, Suppl 1, S11523, 2024, doi: 10.1117/1.JBO.29.S1.S11523.

[22] D. C. Garrett and L. V. Wang, "Acoustic sensing with light," *Nat. Photonics*, vol. 15, no. 5, pp. 324–326, 2021, doi: 10.1038/s41566-021-00804-z.

[23] C. Pieters *et al.,* "Photoacoustic raster scan imaging using an optomechanical ultrasound sensor in silicon photonics," in *Photons Plus Ultrasound: Imaging and Sensing 2022*, San Francisco, United States, 2022, p. 85.

[24] F. Knieling, S. Lee, and V. Ntziachristos, "A primer on current status and future opportunities of clinical optoacoustic imaging," *npj Imaging*, vol. 3, no. 1, 2025, doi: 10.1038/s44303-024-00065-9.

[25] V. Ntziachristos, "Addressing unmet clinical need with optoacoustic imaging," *Nat Rev Bioeng*, vol. 3, no. 3, pp. 182–184, 2025, doi: 10.1038/s44222-024-00242-w.

[26] J. Aguirre *et al.,* "Precision assessment of label-free psoriasis biomarkers with ultra-broadband optoacoustic mesoscopy," *Nat Biomed Eng*, vol. 1, no. 5, 2017, doi: 10.1038/s41551-017-0068.

[27] H. He *et al.,* "Fast raster-scan optoacoustic mesoscopy enables assessment of human melanoma microvasculature in vivo," *Nature communications*, vol. 13, no. 1, p. 2803, 2022, doi: 10.1038/s41467-022-30471-9.

[28] S. Huang *et al.,* "Non-invasive optoacoustic imaging of dermal microcirculatory revascularization in diet-induced obese mice undergoing exercise intervention," *Photoacoustics*, vol. 38, p. 100628, 2024, doi: 10.1016/j.pacs.2024.100628.

[29] M. Omar, J. Gateau, and V. Ntziachristos, "Raster-scan optoacoustic mesoscopy in the 25-125 MHz range," *Optics letters*, vol. 38, no. 14, pp. 2472–2474, 2013, doi: 10.1364/OL.38.002472.

[30] A. Rosenthal, V. Ntziachristos, and D. Razansky, "Optoacoustic methods for frequency calibration of ultrasonic sensors," *IEEE transactions on ultrasonics, ferroelectrics, and frequency control*, vol. 58, no. 2, pp. 316–326, 2011, doi: 10.1109/TUFFC.2011.1809.

[31] A. Penttinen and M. Luukkala, "The impulse response and pressure nearfield of a curved ultrasonic radiator," *J. Phys. D: Appl. Phys.*, vol. 9, no. 10, pp. 1547–1557, 1976, doi: 10.1088/0022-3727/9/10/020.

[32] M. Seeger, D. Soliman, J. Aguirre, G. Diot, J. Wierzbowski, and V. Ntziachristos, "Pushing the boundaries of optoacoustic microscopy by total impulse response characterization," *Nature communications*, vol. 11, no. 1, p. 2910, 2020, doi: 10.1038/s41467-020-16565-2.

[33] C. Zhang, K. Maslov, J. Yao, and L. V. Wang, "In vivo photoacoustic microscopy with 7.6-μm axial resolution using a commercial 125-MHZ ultrasonic transducer," *Journal of biomedical optics*, vol. 17, no. 11, 116016-1 - 116016-6, 2012, doi: 10.1117/1.JBO.17.11.116016.1.

[34] T. J. Allen, O. Ogunlade, E. Zhang, and P. C. Beard, "Large area laser scanning optical resolution photoacoustic microscopy using a fibre optic sensor," *Biomedical optics express*, vol. 9, no. 2, pp. 650–660, 2018, doi: 10.1364/BOE.9.000650.

[35] T. Harary, M. Nagli, N. Suleymanov, I. Goykhman, and A. Rosenthal, "Large-field-of-view optical-resolution optoacoustic microscopy using a stationary silicon-

photonics acoustic detector," *Journal of biomedical optics*, vol. 29, Suppl 1, S11511, 2024, doi: 10.1117/1.JBO.29.S1.S11511.

[36] R. Cao *et al.,* "Optical-resolution photoacoustic microscopy with a needle-shaped beam," *Nature photonics*, vol. 17, no. 1, pp. 89–95, 2023, doi: 10.1038/s41566-022-01112-w.

[37] Y. Hu, Z. Chen, L. Xiang, and Da Xing, "Extended depth-of-field all-optical photoacoustic microscopy with a dual non-diffracting Bessel beam," *Optics letters*, vol. 44, no. 7, pp. 1634–1637, 2019, doi: 10.1364/OL.44.001634.

[38] N. Uluç *et al.,* "Non-invasive measurements of blood glucose levels by time-gating mid-infrared optoacoustic signals," *Nature metabolism*, vol. 6, no. 4, pp. 678–686, 2024, doi: 10.1038/s42255-024-01016-9.

[39] S. Shekhar *et al.,* "Roadmapping the next generation of silicon photonics," *Nature communications*, vol. 15, no. 1, p. 751, 2024, doi: 10.1038/s41467-024-44750-0.

[40] G. Roelkens *et al.,* "Present and future of micro-transfer printing for heterogeneous photonic integrated circuits," *APL Photonics*, vol. 9, no. 1, 2024, doi: 10.1063/5.0181099.

[41] Y. de Koninck *et al.,* "GaAs nano-ridge laser diodes fully fabricated in a 300-mm CMOS pilot line," *Nature*, vol. 637, no. 8044, pp. 63–69, 2025, doi: 10.1038/s41586-024-08364-2.

A. Prebeck received his B.Eng. in electrical engineering and information's technology as well as his M.Eng. in electrical and microsystems engineering from the University of Applied Sciences OTH Regensburg, Germany. Afterwards, he joined Osram OptoSemiconductors / ams Osram as a R&D engineer focusing on chip design for InGaN based light emitting diodes. Currently, he is engaged as a doctoral researcher at the Institute for Biological and Medical Imaging at the Helmholtz Zentrum in Munich, Germany, and the Chair for Biological Imaging at the Technical University of Munich, focused on optoacoustic spectroscopy for sensing of metabolites.

V. Ntziachristos received his Ph.D. in electrical engineering from the University of Pennsylvania, USA. After his Ph.D, he held a postdoctoral position at the Center for Molecular Imaging Research at Harvard Medical School. Afterward, he became an Instructor and then an Assistant Professor and Director at the Laboratory for Bio-Optics and Molecular Imaging at Harvard University and Massachusetts General Hospital, Boston, USA. Currently, he is the director of the Institute for Biological and Medical Imaging at the Helmholtz Zentrum in Munich, Germany, as well as a Professor of Electrical Engineering, Professor of Medicine, and Chair for Biological Imaging at the Technical University of Munich. His work focuses on novel, innovative optical and optoacoustic imaging modalities for studying biological processes and diseases, as well as the translation of these findings into the clinic.

G. Keulemans: received his MSc degree in nanoscience and nanotechnology in 2010 and his Ph.D. degree in electrical engineering in 2019 from KU Leuven, Belgium. Afterwards, he joined imec as R&D engineer focusing on the design, modelling and characterization of opto-mechanical, piezoelectric and acousto-fluidic microsystems. Currently, he is involved as senior engineer in multiple projects related to medical ultrasound, photo-acoustic imaging and spectroscopy and integrated microfluidic actuators and sensors.

U. Stahl: No photograph and biography were available at the time of publication

H. Jans received her Ph.D. in Chemistry from the Catholic University of Leuven, Belgium, and was a visiting scholar at the University of Central Florida. She joined imec as a researcher, focusing on integrating (bio-) applications with emerging technologies. Hilde advanced to Senior Project Manager, overseeing projects on SiN technologies, Raman spectroscopy, and photo-acoustics. She is currently the R&D Manager for the Imaging and Optics team at imec.

X. Rottenberg received his Ph.D. in electrical engineering from KULeuven after a DEA in Theoretical Physics at ULB. He is currently Fellow at imec and Lecturer at ULB and KULeuven. He joined imec in 2000 where he impacted research in RF(-MEMS), optics, acoustics, microsystems, devices and applications modelling & integration. As Fellow at imec, he currently leads the Wave-Based Sensing and Actuation (WSA) activities, working on photonics, phononics, M/NEMS, photonics for quantum systems and in particular quantum sensing. He contributed to the launch of several ventures some of which he co-founded, e.g. Pulsify Medical and SWAVE Photonics.

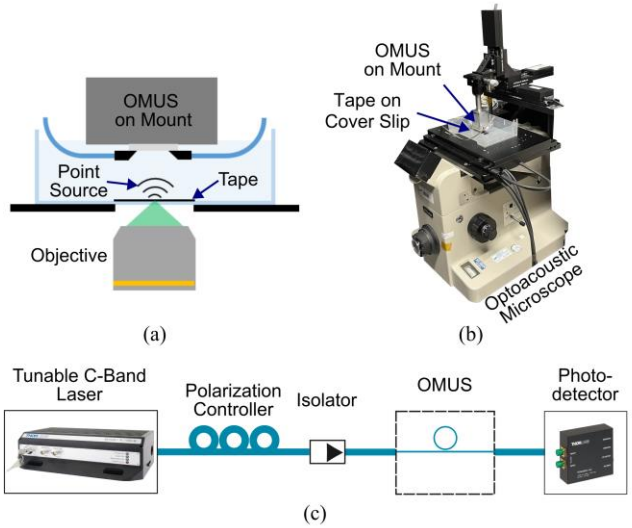

Fig. 1. (a) Schematic representation and (b) photograph of the optical resolution optoacoustic microscope used to create a broadband acoustic point source by focusing light pulses onto a thin vinyl tape. (c) The optical readout system used to interface with the opto-mechanical micromachined ultrasound sensor (OMUS) is shown as a schematic.

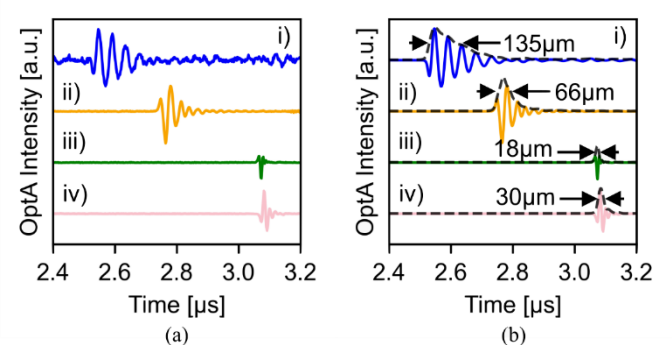

Fig. 2. Impulse response measurements of an opto-mechanical micromachined ultrasound sensor (OMUS) and three single element focused piezoelectric ultrasound transducers (FPUTs) in the time domain. i: OMUS, ii: 25 MHz piezocomposite, iii: 50 MHz $LiNbO_3$, iv: 25 MHz $LiNbO_3$. (a) Raw impulse response measurements (b) averaged impulse response measurements allow for estimations of the axial point spread function (PSF) of both the OMUS and FPUTs (dashed lines). The width of the axial PSF is denoted for each detector (black arrows).

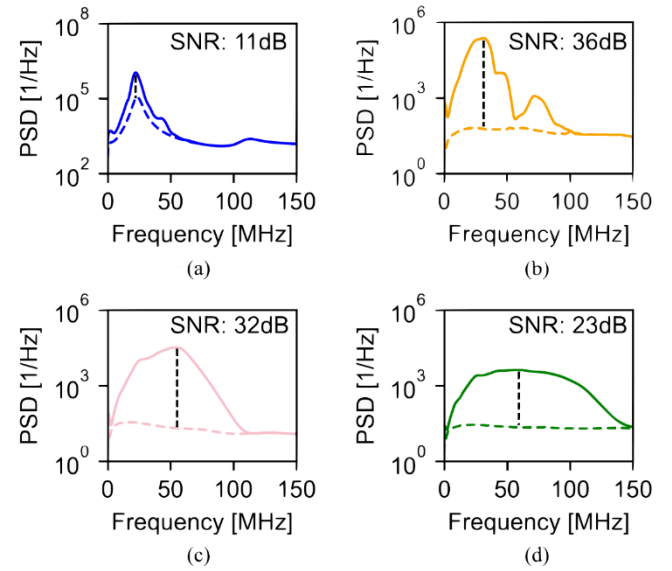

Fig. 3. Impulse response measurements of an opto-mechanical micromachined ultrasound sensor (OMUS) and three single element focused piezoelectric ultrasound transducers (FPUTs) in the frequency domain. (a): OMUS, (b): 25 MHz piezocomposite, (c): 25 MHz $LiNbO_3$, (d): 50 MHz $LiNbO_3$. The power spectral density (PSD) of the raw optoacoustic transients plotted in Fig. 2a (solid lines) as well as system noise preceding every transient (dashed lines) are shown. Frequencies with the highest signal-to-noise ratio (SNR) are marked and their respective SNR values given.

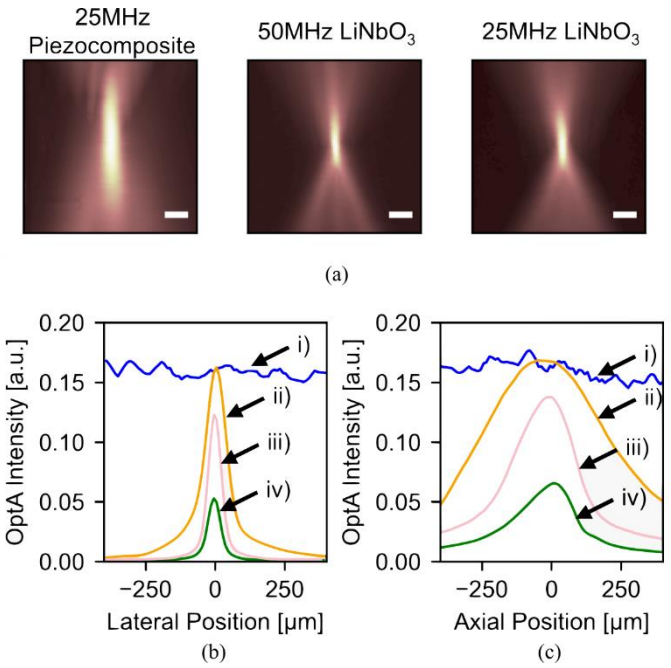

Fig. 4. Spatial characterization of an opto-mechanical micromachined ultrasound sensor (OMUS) and three single element focused piezoelectric ultrasound transducers (FPUTs). i: OMUS, ii: 25 MHz piezocomposite, iii: 25 MHz $LiNbO_3$, iv: 50 MHz $LiNbO_3$. (a) Sensitivity fields of three FPUTs. Scale bars are 100 µm. (b-c) Spatial sensitivity when scanning a point source laterally (b) or axially (c) in front of the detectors.

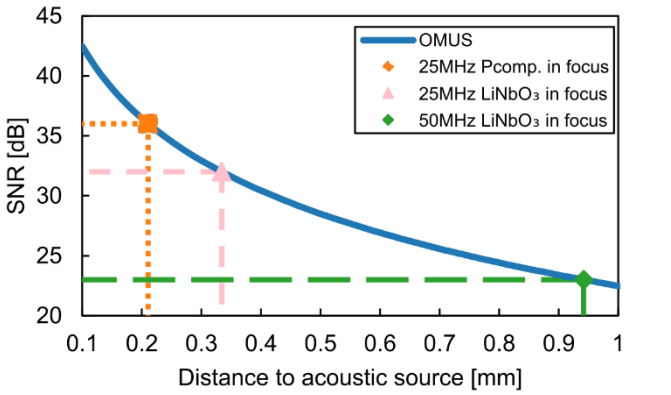

Fig. 5. Extrapolated signal-to-noise ratio (SNR) crossover point of an opto-mechanical micromachined ultrasound sensor (OMUS) and different single element focused piezoelectric ultrasound transducers (FPUTs). Extrapolating the OMUS' SNR from the peak SNR measurement (Fig. 3a) shows that the OMUS' SNR could potentially increase close to the acoustic source, surpassing the best possible peak SNR of the FPUTs at crossover-distances between 0.2 mm and 1.0 mm, depending on the specific FPUT.

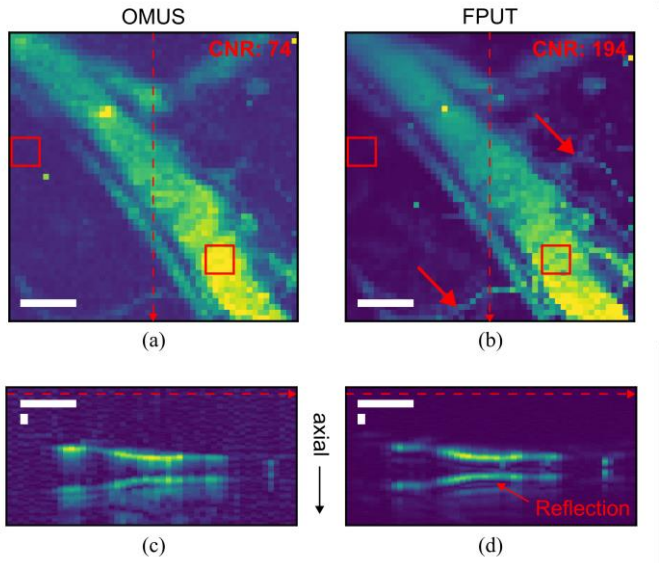

Fig. 6. Micrographs of mouse ear vasculature recorded ex-vivo using either (a) an opto-mechanical micromachined ultrasound sensor (OMUS) or (b) a 25 MHz piezocomposite single element focused piezoelectric ultrasound transducer (FPUT) as detectors within an optical resolution optoacoustic microscope. Small microvasculature, which is clearly visible using the FPUT (indicated by red arrows) is nearly lost in the noise when imaged using the OMUS. Red squares mark the regions used for contrast-to-noise ratio (CNR) calculations. Side views created from B-planes taken along the dashed arrows in panels (a) and (b) show how the (c) OMUS' limited bandwidth results in stronger axial smoothing compared to the (d) FPUT. Acoustic reflection due to the microscopy slide creates an axial mirror image of the vessel. Scale bars are 100 µm.

TABLE I
COMPARISON OF THE OPTO-MECHANICAL MICROMACHINED ULTRASOUND SENSOR (OMUS) TO OTHER DETECTORS

Type	Approx. Area [mm²]	f_c [MHz]	F-BW [%]	NEPD [mPa/√Hz]	Ref.
OMUS	$3.1 \cdot 10^{-4}$	26	63	1.3	[16]
	$1.8 \cdot 10^{-4}$	44	86	2.3	
Photonic detectors from recent publications					
π-WBG	$1.0 \cdot 10^{-7}$	~120	~192	9.0	[12]
π-WBG	$7.7 \cdot 10^{-1}$	100	150	2.2	[5]
Chalcogenide MRR	$1.3 \cdot 10^{-3}$	~95	~184	2.2	[11]
SiN MRR	$7.1 \cdot 10^{-4}$	~74	~155	7.0	[10]
Piezoelectric detectors from recent publications					
PVDF-TrFE	28.3	~17	~200	~0.17	[18]
PVDF	28.3	~19	~200	~0.30	
$LiNbO_3$	31.0	30	21	0.058	[17]
$LiNbO_3$	31.0	30	64	0.058	
Commercially available piezoelectric detectors from Olympus					
V212-BC-RM	28.0	20	187	0.19	[18]
V324-SU	28.0	25	30	0.10	
V214-BC-RM	28.0	50	80	0.19	

Values marked with "~" were extracted from graphs or estimated from other reported values. (Approx.: approximate, f_c: center frequency, F-BW: fractional bandwidth, NEPD: noise equivalent pressure density, Ref.: reference, WBG: waveguide Bragg grating, MRR: microring resonator, SiN: silicon nitride, PVDF: polyvinylidene fluoride, TrFE: trifluoroethylene, $LiNbO_3$: lithium niobate)

TABLE II
SUMMARY OF CHARACTERIZATION RESULTS

Characteristic	OMUS	FPUT 1	FPUT 2	FPUT 3
Sensitive Element	Si-Photonics	Piezocomposite	$LiNbO_3$	$LiNbO_3$
Approx. Active Area [mm²]	0.0003	26.0	12.6	12.6
PSF Width [µm] [a]	135	66	18	30
SNR [dB]	11	36	23	32
Center Frequency [MHz]	22.9	28.3	63.2	46.2
-6dB Bandwidth [MHz]	9.0	19.1	88.5	45.5
Fractional Bandwidth [%]	39.3	67.5	140.0	98.5
Axial Focus Width [µm] [a]	omni-directional	565.8	251.6	277.2
Lateral Focus Width [µm] [a]	omni-directional	92.9	54.8	57.1
SNR Crossover Distance [mm]	-	0.21	0.94	0.33

[a] Widths were determined as full-width-half-maximum values. (OMUS: opto-mechanical micromachined ultrasound sensor, FPUT: single element focused piezoelectric ultrasound transducer, $LiNbO_3$: lithium niobate, SNR: signal-to-noise ratio, PSF: point-spread-function)